Comparison of Acoustic Noise and Vibration in Ball-Bearing-Supported Motors and One-Axis Actively Positioned Single-Drive Bearingless Motor With Two Radial Permanent-Magnet Passive Magnetic Bearings

THEERAPHONG SRICHIANGSA [1] (Member, IEEE), **SURYA NARAYANA GUNDA**[2],
HIROYA SUGIMOTO [3] (Member, IEEE), **YUSUKE FUJII** [2] (Member, IEEE),
KYOHEI KIYOTA [2] (Member, IEEE), **JUNICHI ASAMA** [4] (Member, IEEE), **AND AKIRA CHIBA** [2] (Fellow, IEEE)

[1]Department of Electrical Engineering, Faculty of Engineering at Sriracha, Kasetsart University, 20230 Chonburi, Thailand
[2]Department of Electrical and Electronic Engineering, Tokyo Institute of Technology, 152-8550 Tokyo, Japan
[3]Department of Electrical and Electronic Engineering, Tokyo Denki University, 120-8551 Tokyo, Japan
[4]Department of Mechanical Engineering, Shizuoka University, 432-8561 Shizuoka, Japan

CORRESPONDING AUTHOR: THEERAPHONG SRICHIANGSA (e-mail: srichiangsa.t@belm.ee.titech.ac.jp)

ABSTRACT This study experimentally investigates the acoustic noise, vibration, and power consumption in a one-degree-of-freedom actively positioned single-drive bearingless motor, which has radial passive magnetic bearings (RPMBs) and compared to an identical stator part and rotor shaft with radial mechanical ball bearings. For the experiment, three test motors were set up: (a) a bearingless motor with two RPMB, (b) a motor with two ball bearings without an axial preload, and (c) a motor with two ball bearings with an axial preload. Motor (a) under test had one-axis active positioning and the radial movements were supported by RPMB made of cylindrical permanent magnets. Conversely, in motors (b) and (c), the radial and axial movements were supported by ball bearings, and there was no production of active axial force. The experimental results confirmed that the levels of acoustic noise, stator vibration, and input power consumption were significantly lower in motor (a) than those in motors (b) and (c). In the analysis section, dynamic models of the bearingless motor with RPMB and motor with ball bearings were designed and simulated using MATLAB \ Simulink. The low radial stiffness in RPMB was found to contribute to acoustic noise and vibration reductions. Thus, this article presents an example of a one-degree-of-freedom actively positioned bearingless motor with RPMB that realizes reductions of acoustic noise, stator vibration, and input power consumption.

INDEX TERMS Acoustic noise reduction, bearingless motor, power consumption, radial passive magnetic bearings (RPMB), vibration reduction.

I. INTRODUCTION

Bearingless motors can generate rotating motor torque and active radial or axial magnetic suspension forces. These motors have the advantages of being lubricant-free and having non-contact magnetic suspensions, which are beneficial for several industrial applications, such as in centrifugal liquid pumps for highly pure processes [1], artificial hearts [2], mixing devices [3], rotating stages [4], flywheel energy storages [5], compressors [6], [7], cooling fans [8], and others [9].

Bearingless motors are categorized according to the number of actively positioned degrees of freedom (DOF). A five-DOF actively positioned bearingless motor provides reliable

magnetic suspensions. However, it requires numerous sensors and power electronic devices, including five displacement sensors, three units of three-phase inverters, and one single-phase inverter [10], [11]. Thus, two-DOF actively positioned bearingless motors have been proposed to reduce the size and cost of noncontact magnetic suspensions [12], [13], where the remaining three DOF were passively suspended. Moreover, one-DOF actively positioned magnetic bearing motors have also been proposed, which require only one single-phase and three-phase inverter each to generate the active axial suspension force and motor torque [14], [15]. Further simplification of one-DOF active positioning has been investigated [16], [17], and single-drive bearingless motors have been proposed by some of our authors [8], [18], [19], which require only one three-phase inverter, without any additional single-phase inverters.

The rotational speeds of the one-DOF bearingless motors have been improved. In [20], a test single-drive bearingless motor with a rotational speed of 16 000 r/min was reported. Recently, some of our authors have developed a test bearingless motor, which achieved a rotational speed of 30 000 r/min [21]. The basic motor design and its characteristics were reported; however, reports on the reduction of acoustic noise and stator vibration were excluded. Although bearingless motors have been developed for more than 30 years, no experimental reports on the reduction of acoustic noise and stator vibration acceleration have been reported.

Acoustic noise and vibration are the main issues in typical rotating electrical motors with mechanical ball-bearing supports. Noise and vibrations are generated by sources such as radial force variation, stator deformation including mode 0, 2, or higher, magnetostriction, stator, and rotor eccentric displacement, and rotor shaft unbalance mass. In high-speed motors, vibration, and acoustic noise generally are originated from the unbalance mass of the rotor shaft. Yan et al. [22] analyzed the radial force acting on the stator teeth corresponding to the rotor eccentricity in conventional and bearingless switched reluctance motors and observed a reduction in vibration in the simulation results. Sinervo et al. [23] demonstrated suppression of the rotor vibration in a bearingless induction motor using stator damper winding. However, no reports on the stator vibration reduction were presented in [22] and [23].

This study conducted experimental verifications of acoustic noise and vibration reductions in a one-DOF actively positioned single-drive bearingless motor with radial passive magnetic bearings (RPMB), and the experimental results were compared to those of motors with ball bearings. Rotor radial movements of the bearingless motor were supported by RPMB made of permanent magnet (PM) rings. However, the rotor axial movements were actively regulated by the d-axis current of a three-phase inverter. Thus, the bearingless motor could achieve a full noncontact suspension. Since the RPMB allowed rotor shaft movement in the radial direction, the stator radial vibration was reduced at a high rotational speed. As the stator vibration acceleration reduced, the overall acoustic noise was found to reduce by approximately -10 to -20 dBA
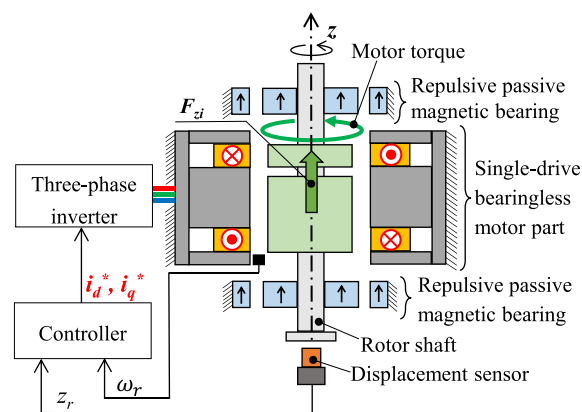

FIGURE 1. Basic structure of the single-drive bearingless motor with RPMBs and its drive system.

when compared to those of two motors with ball bearings. The two motors with ball bearings did not have active force generation, and only the rotating torque was actively controlled. In addition, the input power consumption of the bearingless motor was reduced at high rotational speeds. Furthermore, dynamic models of a bearingless motor with RPMB and motor with ball bearings were modeled using MATLAB \ Simulink. It was observed that the low radial stiffness in the RPMB contributed to the acoustic noise and vibration reduction.

II. BASIC CONCEPTS
This section presents the basic structure of a one-DOF actively positioned single-drive bearingless motor with RPMB. In addition, the basic rotor shaft support in the single-drive bearingless motor with RPMB and motor with mechanical ball bearings is discussed.

A. BASIC STRUCTURE OF A SINGLE-DRIVE BEARINGLESS MOTOR WITH RPMB
Fig. 1 shows a simplified structure of the proposed single-drive bearingless motor [21]. The motor structure comprises a single-drive bearingless motor with two sets of RPMB made of two PM rings with small and large diameters. The two sets of RPMB provide radial passive stabilization at both ends of the rotor shaft. The motor consists of three stator core layers, two rotor layers, and a set of three-phase concentrated short-pitch windings. The motor generates an active axial force and a rotating torque using the d- and q- axis currents, respectively. In addition, a displacement sensor is installed at the bottom of the rotor shaft to detect the rotor axial displacement z_r for an active axial magnetic suspension. The controller generates d- and q- axis currents based on the rotor axial position z_r, rotor rotational position θ_r, and rotor angular speed ω_r.

B. BASIC CONCEPTS OF RADIAL ROTOR SHAFT SUSPENSION
Fig. 2(a) shows the rotor shaft suspension based on RPMB in the radial direction. The rotor and stator PMs were magnetized
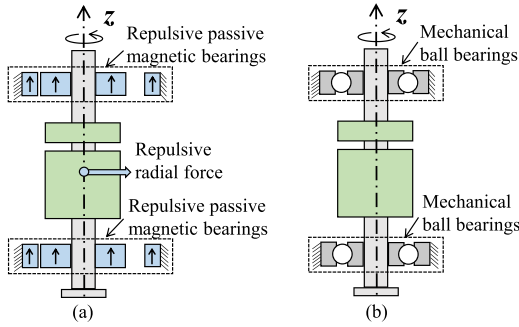
FIGURE 2. Basic principle of radial suspension of the rotor shaft with (a) RPMB and (b) mechanical ball bearings.

m_r, m_s is the rotor, and stator masses
x_r, x_s is the rotor, and stator displacements
k_{rs}, d_{rs} is the coupled rotor-stator stiffness, and damping
k_s, d_s is the stator stiffness, and damping
F_{cx}, F_{cy} is the centrifugal force in x- and y- directions
e_u is the rotor eccentricity

FIGURE 3. Two mass-spring systems representing the rotor and stator movements in the x-direction.

in the axial direction, as indicated by the arrows. When the rotor shaft displaces in the radial direction, a repulsive force is generated by the PM rings and the rotor shaft can be passively stabilized. In the test motor, the rotor could move in a 1 mm range. Fig. 2(b) shows the rotor shaft suspension based on mechanical ball bearings. The rotor can be precisely positioned in the radial direction owing to the high stiffness property of the ball bearings. However, a high radial stiffness corresponds to a high radial stator vibration acceleration. Generally, the rotor shaft has an unbalanced mass that generates a synchronous shaft movement, which is usually suppressed by the ball bearings. However, the RPMB allows shaft movement, thus, reducing the stator vibration acceleration. Consequently, the acoustic noise reduces.

III. BASIC PRINCIPLE OF ROTOR AND STATOR VIBRATIONS AND MATLAB/SIMULATION RESULTS

This section presents a two mass-spring system representing the rotor and stator vibrations of a motor. Furthermore, the motion equations and a block diagram of the rotor and stator are presented. MATLAB \ Simulink was used to investigate the vibration characteristics of the bearingless motor with RPMB and typical motor with ball bearings, the simulation results are presented and discussed.
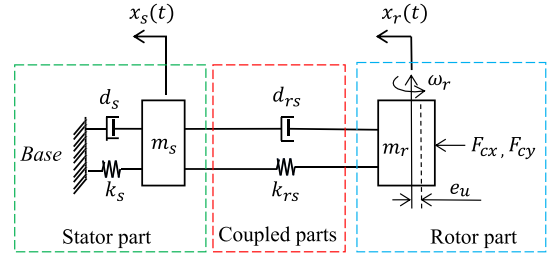
A. TWO MASS-SPRING SYSTEM AND MOTION EQUATION

Fig. 3 shows a two mass-spring system representing the rotor and stator vibrations, where m_r and m_s represent the rotor and stator masses (kg), respectively. The parameters d_{rs}, d_s, k_{rs}, and k_s represent the coupled rotor-stator damping, stator damping, coupled rotor-stator radial stiffness, and stator radial stiffness, respectively. e_u represents the eccentricity of the principal axis due to the mass imbalance. Additionally, F_{cx} and F_{cy} represent the centrifugal forces due to the eccentricity of rotor mass. The centrifugal forces are given as
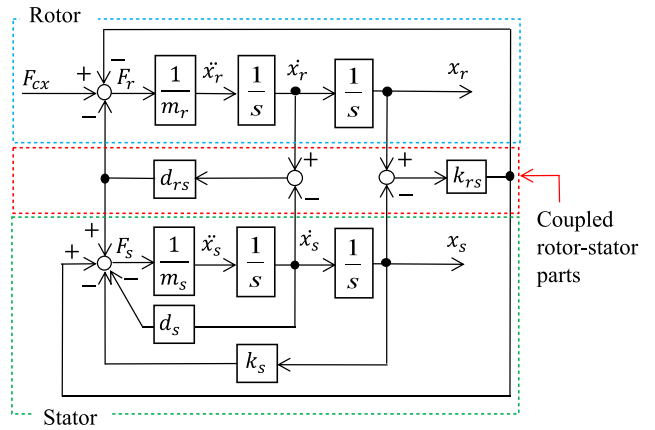
$$F_{cx} = e_u m_r \omega_r^2 cos(\omega_r t) \quad (1)$$

$$F_{cy} = e_u m_r \omega_r^2 \sin(\omega_r t). \quad (2)$$

The motion equations in the x-direction can be written as

F_r, F_s is the radial force acting on the rotor and stator.
$x_s, \dot{x}_s, \ddot{x}_s$ are the stator displacement, velocity, vibration acceleration
$x_r, \dot{x}_r, \ddot{x}_r$ are the rotor displacement, velocity, vibration acceleration

FIGURE 4. Block diagram of rotor and stator movements in the x-direction for motors with ball bearings and with RPMBs.

$$m_r \ddot{x}_r = F_{cx} - d_{rs}(\dot{x}_r - \dot{x}_s) - k_{rs}(x_r - x_r) \quad (3)$$

$$m_s \ddot{x}_s = d_{rs}(\dot{x}_1 - \dot{x}_s) - d_s \dot{x}_s + k_{rs}(x_r - x_s) - k_s x_s. \quad (4)$$

where x_r and x_s are defined as the rotor and stator displacements, respectively. Then, $\dot{x}_r$ and $\dot{x}_s$ represent the rotor and stator velocities, respectively. In addition, $\ddot{x}_r$ and $\ddot{x}_s$ are the rotor and stator vibration accelerations, respectively. In this study, the rotor displacement x_r and stator vibration acceleration $\ddot{x}_s$ are important variables under consideration.

B. BLOCK DIAGRAM OF ROTOR AND STATOR MOVEMENTS

Fig. 4 shows the block diagram of the rotor-stator dynamics in the x-direction based on (3) and (4). Both the ball bearing and RPMB suspensions are represented by their block diagrams for simulation. The parameters used in the simulations are listed in Table 1. The relationship between natural frequency

TABLE 1. Key Parameters of the Two Motors for Simulation in MATLAB/Simulink Simulation

Parameter	$RPMB^{(a)}$	$Ball\ bearings^{(b)}$	Unit
Rotor mass, m_r	0.055	0.055	kg
Stator mass, m_s	0.20	0.20	kg
Rotor-stator stiffness, k_{rs}	6.5×10^3	650×10^3	N/m
Rotor-stator damping, d_{rs}	0.0026	0.26	N s/m
Stator stiffness, k_s	650×10^3	650×10^3	N/m
Stator damping, d_s	0.26	0.26	N s/m

$^{(a)}$bearingless motor with RPMB. $^{(b)}$motor with ball bearings.

f_{rc}, coupled rotor-stator radial stiffness k_{rs}, and rotor mass m_r is expressed as

$$f_{rc} = \frac{1}{2\pi}\sqrt{\frac{k_{rs}}{m_r}} \qquad (5)$$

The masses m_r and m_s were measured using a digital weighing scale, while the natural frequency f_{rc} was measured using the waveforms of the radial shaft movements detected by laser sensors. The coupled rotor-stator radial stiffness k_{rs} of the bearingless motor with RPMB can be calculated from

$$k_{rs} = (f_{rc} \times 2\pi)^2 \times m_r \qquad (6)$$

The coupled rotor-stator damping d_{rs} of the bearingless motor with RPMB was calculated with reference to [24]. Conversely, the coupled rotor-stator radial stiffness k_{rs} and damping d_{rs} of the motor with ball bearings were roughly estimated to be 100 times higher than in the bearingless motor with RPMB. The stator radial stiffness k_s and damping d_s were set identical to k_{rs} and d_{rs}, respectively. These values of k_s and d_s remained unchanged with the use of ball bearings or RPMB.

C. MATLAB \ SIMULINK SIMULATION RESULTS

Fig. 5(a) and (b) shows the simulation results of the shaft rotational speed N_r, rotor displacement x_r, and stator vibration acceleration $\ddot{x}_s$ of motors with ball bearings and RPMB, respectively. At a speed of 25 000 r/min, the rotor displacement x_r was small, but the stator vibration acceleration $\ddot{x}_s$ was large in the motor with ball bearings. Whereas the rotor displacement x_r was large, the stator vibration acceleration $\ddot{x}_s$ was reduced by 98% in the motor with RPMB when compared to that in the motor with ball bearings. Since the stator vibration acceleration $\ddot{x}_s$ depends on the radial force F_s acting on the stator, the reductions in the stator vibration acceleration can be explained. For a high F_s, $\ddot{x}_s$ is also high. Thus, F_s is expressed as

$$F_s = k_{rs}(x_r - x_s) + d_{rs}(\dot{x}_r - \dot{x}_s) - k_s x_s - d_s \ddot{x}_s. \qquad (7)$$

Although the values of k_s, d_s, m_r, and m_s in the motors with ball bearings and RPMB were identical, k_{rs} and d_{rs} in the motor with ball bearings had values that were 100 times higher than those in the bearingless motor with RPMB. The value of x_r in the bearingless motor with RPBM was 4 times
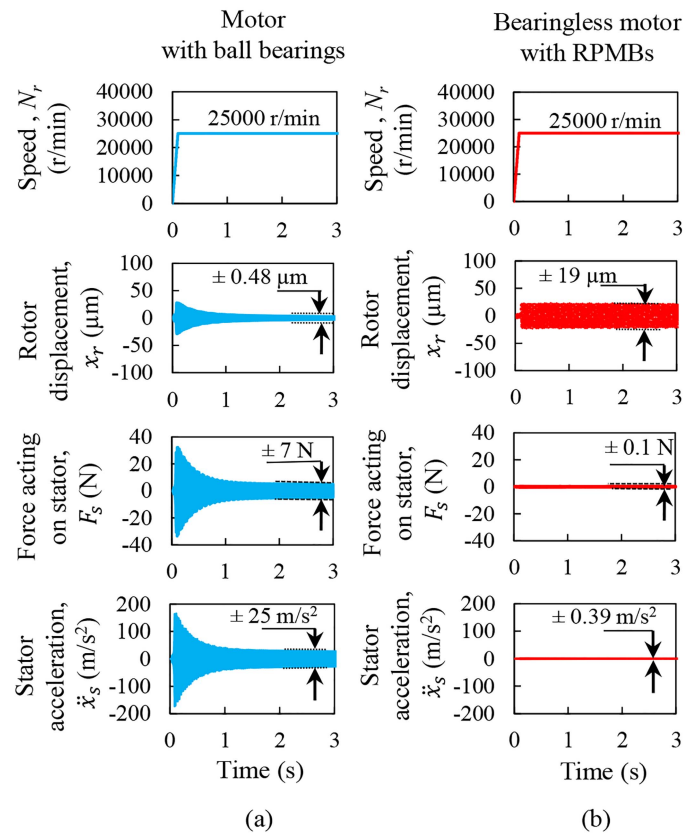

FIGURE 5. MATLAB/Simulink simulation results in x- directions of (a) motor with ball bearings and (b) bearingless motor with RPMBs at acceleration speed of 25 000 r/min.

higher than that in the motor with ball bearings, as shown in Fig. 5. Despite the higher value of x_r in the bearingless motor, the value of F_s was significantly reduced because k_{rs} had a small value. Therefore, the stator vibration acceleration $\ddot{x}_s$ was reduced, thus reducing the acoustic noise.

IV. MOTOR PROTOTYPE AND PRINCIPLE OF ROTATING TORQUE AND ACTIVE AXIAL FORCE GENERATION

This section discusses the fabricated motor prototypes used in experiments. Experimental setups of three variations in the test motor are presented. In addition, a detailed three-dimensional computer-aided design (3D-CAD) model, specification, and winding layout of the bearingless motor are presented. Additionally, the principle of torque and active axial force generation, including voltage equation of the single-drive bearingless motor, are discussed.

A. FABRICATED MOTOR PROTOTYPE

Fig. 6(a) shows a photograph of the motor prototype. A one-axis vibration acceleration sensor (PV-91 C) was installed on the outer surface of the center stator core to detect the stator vibration acceleration. Fig. 6(b) shows the rotor shaft for operation in the bearingless motor with RPMB. The rotor consists of two-layer four-pole PMs and two sets of RPMB. The PMs were made of N40SH material. A carbon fiber-reinforced
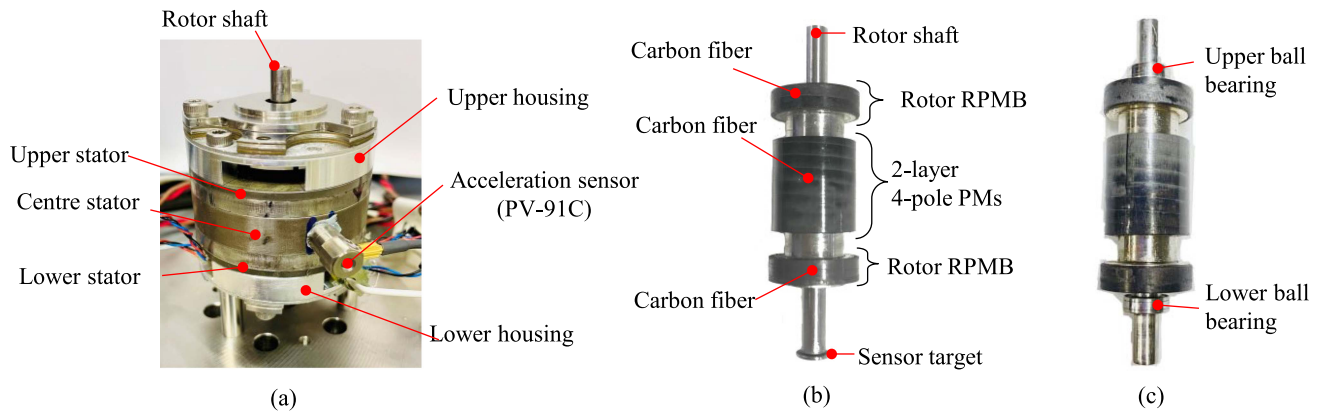
FIGURE 6. Prototype of the test motor: (a) assembled motor, (b) rotor shaft with RPMB, and (c) rotor shaft with ball bearings.
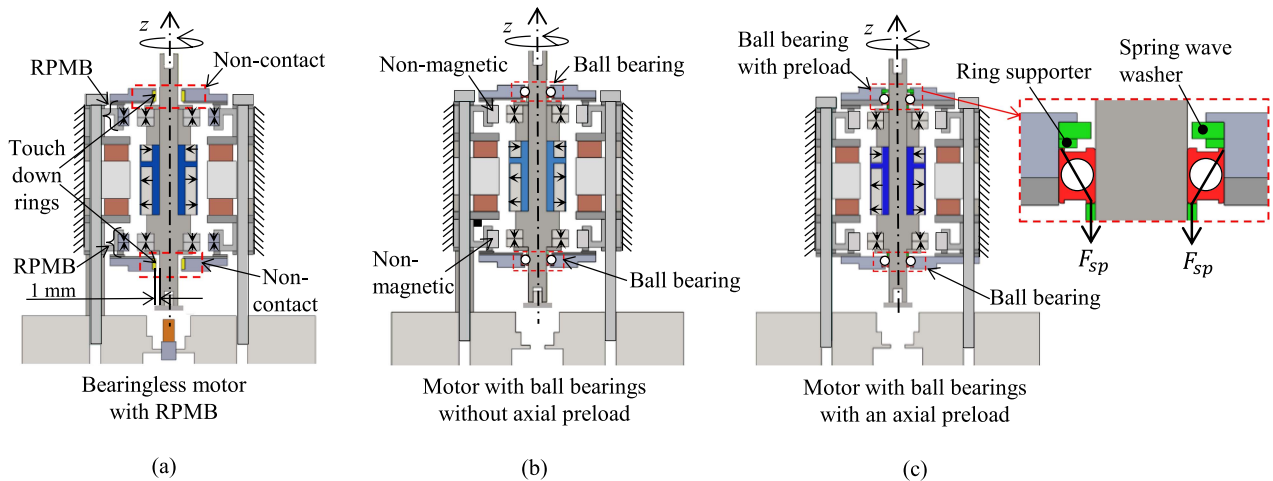

FIGURE 7. Three variations in the test motor: (a) bearingless motor with RPMB; (b) motor with ball bearings without an axial preload; and (c) motor with ball bearings with an axial preload. Since only one rotational shaft was fabricated for the three variations, the unbalance mass was identical.

polymer (CFRP) bandage, seen as the black cylindrical surface, was fixed on the surfaces of the center rotor PMs and PMs of the two sets of RPMB. Fig. 6(c) shows the assembled rotor shaft of a motor with ball bearings, which had two ball bearings added to the top and bottom of the rotor shaft.

B. EXPERIMENTAL SET UP OF THREE TEST MOTORS

Fig. 7(a) shows the test structure of the bearingless motor with noncontact passive magnetic suspensions. Therefore, no physical contact existed in the rotor shaft. Radial movements at both ends of the shaft were supported by RPMB, whereas movement in the axial direction was supported by active axial magnetic suspensions. In addition, the maximum allowable radial distance between the rotor shaft and the stator touch-down ring was 1 mm. Fig. 7(b) shows the test structure of the motor with ball bearings without an axial preload. The rotor shaft was in contact with two mechanical ball bearings. In addition, the stator PMs of the RPMB were removed and replaced with a nonmagnetic material. Fig. 7(c) shows the

test structure of the motor with ball bearings with an axial preload using a spring-wave washer. The spring-wave washer was installed near the top of the rotor shaft to generate the axial spring force F_{sp}, which can reduce the clearance of the ball bearings. Thus, the acoustic noise and vibration can be reduced, although the input power consumption increases.

C. 3D-CAD MODEL AND WINDING CONFIGURATION

Fig. 8 shows the 3D-CAD cross-sectional view of the single-drive bearingless motor prototype, whose details are presented in [21]. Thus, only the outline of the prototype is reviewed in this article. The RPMB was placed near the upper and lower ends of the shaft with two layers of PM rings. The bearingless motor comprised a three-layer stator core, a two-layer four-pole PM rotor, and a set of three-phase concentrated short-pitch windings. Since RPMB generates an unstable axial force, an active axial force is required to stabilize the rotor shaft in the axial direction. As flux strengthening occurred when a positive d-axis current was applied, an increase in
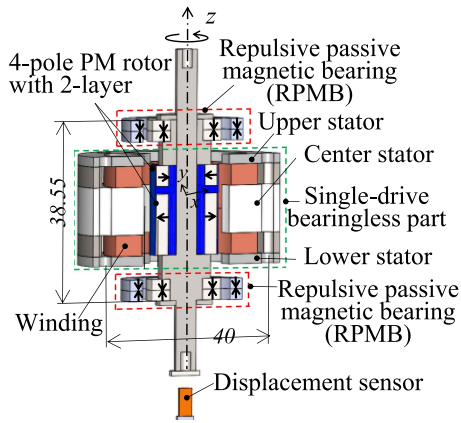
FIGURE 8. 3D-CAD model of the single-drive bearingless motor prototype.
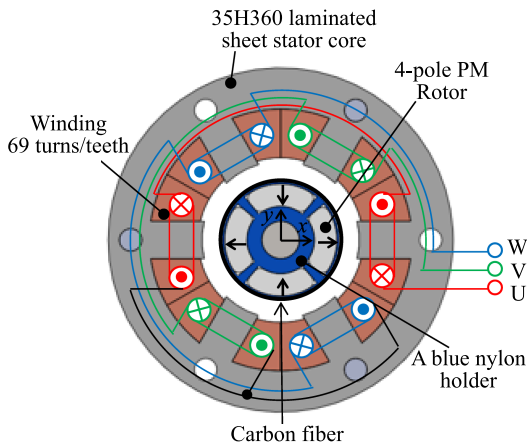
FIGURE 9. Cross-sectional central layer view of the single-drive bearingless motor with three-phase concentrated winding along the *x* and *y* axes.

the fringing flux generated an active axial force because the rotor PM and the upper and lower stator iron cores were not confronted. Thus, the axial active force was proportional to the *d*-axis current.

Fig. 9 shows the cross-sectional central layer view of the single-drive bearingless motor along the *x* and *y* axes. The four PMs of the rotor were magnetized in the parallel radial direction, and were fixed by a blue nylon holder surrounded by carbon fiber. The stator had six teeth, with each tooth holding a concentrated short-pitch winding of 69 turns. The concentrated short-pitch windings were connected in series to realize conventional three-phase windings. Other key parameters and specifications of the motor prototype are listed in Table 2.

D. PRINCIPLE OF ROTATING TORQUE AND ACTIVE AXIAL MAGNETIC SUSPENSION FORCE GENERATIONS

Since the *d*- and *q*-axis voltage equations for the single-drive bearingless motor have been previously derived [25], [26], the

TABLE 2. Key Specifications of the Motor Prototype

Parameters	Value	Unit
DC-link voltage, V_{dc}	48	V
Rated RMS current	1.57	A
Rated power at knee speed of 14 000 r/min	30	W
Rated torque	20.2	mNm
Rated current density	8	A/mm^2

voltage equation is expressed as

$$\begin{bmatrix} v_d \\ v_q \end{bmatrix} = \begin{bmatrix} R + \mathbf{P}L_d & -p\omega_r L_q \\ p\omega_r L_d & R + \mathbf{P}L_q \end{bmatrix} \begin{bmatrix} i_d \\ i_q \end{bmatrix} + \begin{bmatrix} k_\omega \lambda_{m0} \mathbf{P} z_r \\ p\omega_r \lambda_{m0}(1 + k_\omega z_r) \end{bmatrix} \tag{8}$$

where v_d and v_q are the *d*- and *q*-axis voltages, respectively, *R* is the winding resistance per phase, ω_r is the rotor rotational angular speed, *p* is the number of pole pairs, $\mathbf{P}$ is the time-derivative operator of $\dfrac{d}{dt}$, and z_r is the rotor axial position. L_d and L_q are the *d*- and *q*-axis inductances, respectively. i_d and i_q are the *d*- and *q*- axis currents, respectively, k_ω is the coefficient of the rate of change of the *q*-axis induced voltage caused by the rotor axial displacement and λ_{m0} is the nominal flux linkage at $z_r = 0$ mm. The electric power can be calculated from the product of *d*–*q* axis voltages of (8) and *d*–*q* axis currents. Then, the rotating torque *T* and active axial force F_{zi} can be derived as

$$T = p\lambda_{m0}(1 + k_\omega z_r)i_q \tag{9}$$

$$F_{zi} = k_\omega \lambda_{m0} i_d = k_{zi} i_d. \tag{10}$$

In (9), torque constant K_t is equal to $p\lambda_{m0}(1 + k_\omega z_r)$. In (10), the product of k_ω and λ_{m0} is expressed in Wb/m, which can be converted into N/A; thus, $k_\omega \lambda_{m0}$ is equal to the current–force factor k_{zi}. Thus, (9) and (10) suggest that the active axial force and rotating motor torque can be controlled separately by the *d*- and *q*- axis currents, respectively. In addition, the active axial force F_{zi} and torque *T* can be expressed in terms of leading angle β as

$$\begin{bmatrix} F_{zi} \\ T \end{bmatrix} = \sqrt{i_d^2 + i_q^2} \begin{bmatrix} k_{zi} \sin \beta \\ p\lambda_{m0}(1 + k_\omega z_r) \cos \beta \end{bmatrix} \tag{11}$$

where β is the leading angle of armature current from the *q*-axis. During motor operation, the leading angle β varied from $-90°$ to $90°$. Thus, the torque was maximized when $\beta = 0°$, i_q = the rated *q*− axis current value, and $i_d = 0$ A. Conversely, the positive active axial force was maximized when $\beta = -90°$, i_d = the rated *d*-axis current value, and $i_q = 0$ A. β was determined using the *d*- and *q*-axis current references.

Furthermore, bearingless motors generate torque and suspension force simultaneously; thus, the torque density reduces relative to that in the conventional motors. In active radial suspension force bearingless motors, 10–20% of the stator slots are occupied by suspension windings. Thus, 10–20% of torque density reduces relative to that in the conventional motors. In the single-drive bearingless motor of this study,
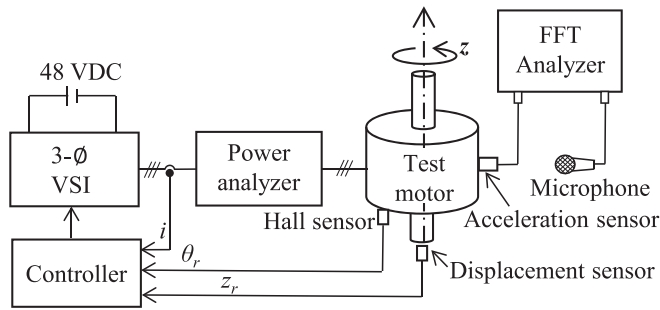
FIGURE 10. Diagram of the measurement system used for measuring the input power, acoustic noise, and stator vibration acceleration.

FIGURE 11. Installation position of the (a) microphone and (b) acceleration sensor relative to the test motor.

17% of the axial length was necessary to generate the axial force, and a 3 mm wide radial air-gap length was required to avoid radial touch-down. However, the air-gap reduced the torque density. Thus, the torque density and axial force were investigated for improvements. The torque density of the first prototype was 0.0084 Nm/l [17]. However, the torque density of this prototype was improved to 0.43 Nm/l. Thus, the improvements of the torque and suspension force densities are one of the main research topics in the field of bearingless machines.

V. MEASUREMENT SYSTEM AND SETUP

This section presents a detailed system for the measurement of input power, acoustic noise, and stator vibration acceleration of three test motors. In addition, details on the control system of the three test motors are discussed.

Fig. 10 shows a diagram of the measurement system used for the measurement of input power, acoustic noise, and stator vibration acceleration. The three-phase input power was measured using a power analyzer (Yokogawa, WT1800) at the output of the three-phase inverter, while an electric microphone (UC-59, RION Co., Ltd.) with preamplifiers (NH-22 A, RION Co., Ltd.) was used to detect acoustic noises. The microphone was connected to a fast Fourier transform analyzer (multifunction measuring system platform SA-A1, RION Co., Ltd.). A one-axis vibration acceleration sensor (PV-91 C, RION Co., Ltd.) was installed on the outer surface of the center stator core and was used to measure the stator vibration acceleration.

Fig. 11(a) shows the installation position of the microphone (UC-59) with the preamplifiers (NH-22 A) relative to the test motor. Since the microphone was aligned to the center position of the test motor, it could detect the radiated acoustic noise of the test motor. The microphone had a frequency range between 10 Hz and 20 kHz and a maximum input sound pressure level of up to 148 dB [27]. Fig. 11(b) shows the cross-sectional view of the stator and the position of the vibration acceleration sensor. The sensor was installed outside the center stator tooth and had a vibration frequency range of 1 Hz to 20 kHz at -50°C to 150 °C. In addition, the sensor offered a maximum measurable acceleration of 5000 m/s^2 [28].
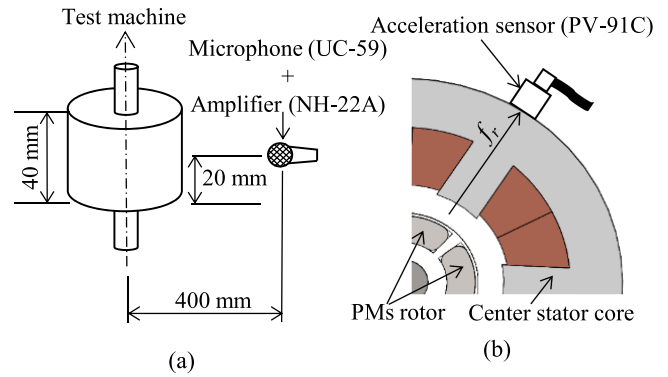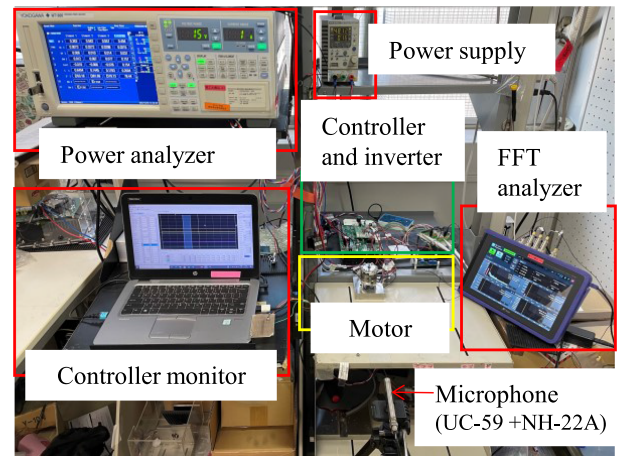

FIGURE 12. Photograph of the actual measurement system used for measuring the input power, acoustic noise, and stator vibration acceleration.
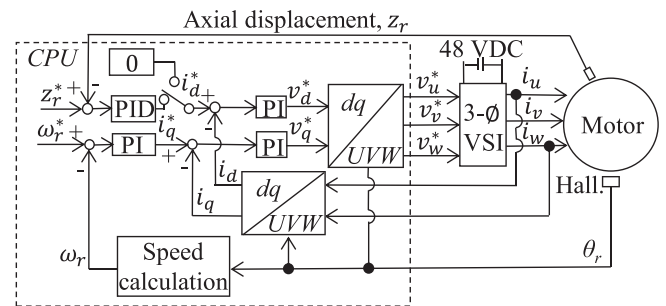

FIGURE 13. Block diagram of the control system for the active axial magnetic suspension and rotational speed regulation.

Fig. 12 shows the experimental workbench, including the test motor, controller monitor, and measurement system, and etc.

Fig. 13 shows the block diagram of the control system for the active axial magnetic suspension and rotational speed regulation. The active axial magnetic suspension gets activated

when the switch selects the output of the proportional–integral–derivative (PID) controller. An axial displacement sensor was installed under the rotor shaft to detect its axial position. Thus, a d-axis reference current i_d^* was generated by the PID controller depending on the error signal between the reference z_r^* and detected z_r rotor axial positions. For testing the motor with ball bearings, the switch selected $i_d^* = 0$. Only the q-axis current gets activated and is used to regulate the rotational angular speed ω_r. The q-axis current reference i_q^* was generated using a proportional–integral (PI) controller.

VI. EXPERIMENTAL RESULTS AND DISCUSSION

This section discusses the experimental results in the (i) acceleration test improvements of the bearingless motor, (ii) power consumption, (iii) stator vibration acceleration, and (iv) acoustic noise of the three test motors.

A. ACCELERATION TESTS OF THE BEARINGLESS MOTOR

An acceleration test with rotational speed ranging from 0 to 20 000 r/min was performed successfully on the proposed single-drive bearingless motor with a stable active axial magnetic suspension control, as presented in [21]. After reaching a rotational speed of 20 000 r/min, the speed was gradually increased in intervals of 1000 r/min until a rotational speed of 30 000 r/min was achieved. An acceleration test with rotational speed ranging from 0 r/min to a high value is one of the challenges in one-DOF actively positioned bearingless motors, while demonstrating the motor performance. Thus, this study also challenged an improvement of the acceleration high-speed test, and an improvement of the acceleration test with rotational speed ranging from 0 to 25 000 r/min was achieved. The improvement was brought about by the increase in the axial gap touch-down length and d-axis current. The axial gap touch-down length was increased from 0.38 to 0.8 mm, while the d-axis current limit was increased from 6.0 to 6.5 A. The proposed single-drive bearingless motor achieved the highest rotational speed from 0 to 25 000 r/min in the acceleration test of this study and the highest operational speed of 30 000 r/min at a steady state in [21] relative to that of the one-DOF actively positioned bearingless motors in the literature review.

Fig. 14 shows the waveforms of the rotor axial displacement z_r, U-phase current i_u, d-axis current i_d, q-axis current i_q, and rotor rotational speed N_r obtained from the acceleration test conducted on the bearingless motor with RPMB. Before acceleration, the rotor shaft was already in the state of magnetic suspension owing to the d-axis current regulation based on the PID controller output. With the activation of the q-axis current, the rotational speed increased as a ramp function and reached 25 000 r/min. Therefore, the bearingless motor with RPMB could achieve a rotational speed of 25 000 r/min and stable magnetic suspension when controlled independently by the q- and d-axis currents, respectively.
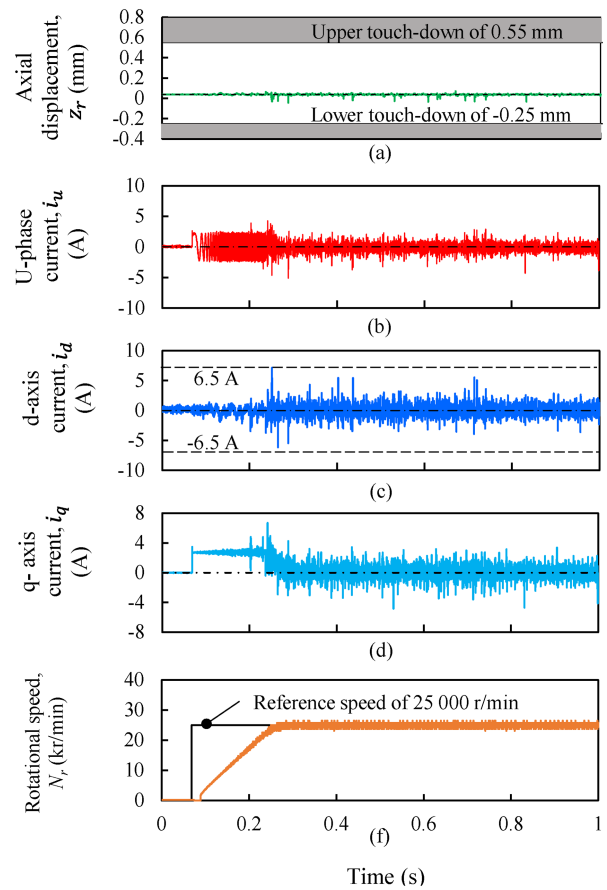

FIGURE 14. Measured waveforms of the (a) rotor axial displacement z_r (b) U-phase current i_u (c) d-axis current i_d (d) q-axis current i_q, and (f) rotor rotational speed N_r.

B. MEASURED INPUT POWER

1) COMPARISON OF MEASURED INPUT POWER IN THREE TEST MOTORS

Fig. 15 shows the measured input power for the three test motors with respect to the rotational speed from 1000 to 25 000 r/min in the no-load test. The input power was low in the bearingless motor from 5000 to 25 000 r/min. At 25 000 r/min, the bearingless motor needs only 2.73 W. In contrast, the test motor with ball bearings needs 11.14 and 4.4 W with and without the axial preload, respectively. However, the input power of the bearingless motor was high at 3000–4000 r/min because of the critical speeds.

2) ESTIMATIONS OF MAGNETIC SUSPENSION LOSS AT KNEE POINT

The power consumed to keep the rotor in an appropriate state of magnetic suspension (magnetic suspension power) was estimated. The output power of the motor was 30 W after the knee speed of 14 000 r/min. However, the output power had increased as the speed increased until the knee point. Direct measurement of magnetic suspension power identification is difficult because the magnetic suspension has no separated
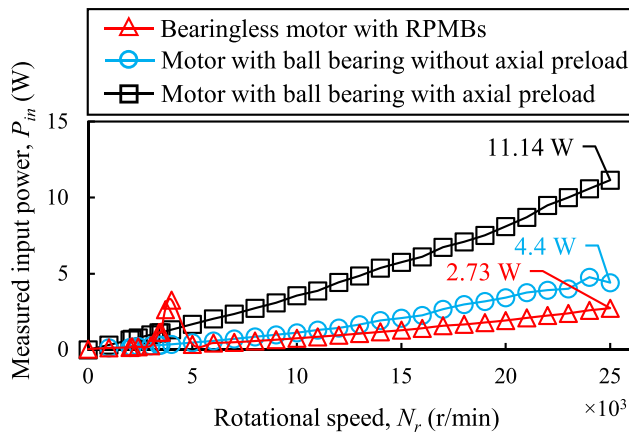
FIGURE 15. Experimentally measured input powers of the three test motors with rotational speeds up to 25 000 r/min.

Medthod	No axial preload[1] (W)	With axial preload[2] (W)
[29][3]	3.40	-
[30][4]	3.57	-
This article[5]	2.7	9.5

[1] ball bearings loss in case of without axial preload.
[2] ball bearings loss in case of with axial preload.
[3] Evaluation of ball bearing losses using (12).
[4] Measurement of ball bearing losses by performing an experimental identification system [30].
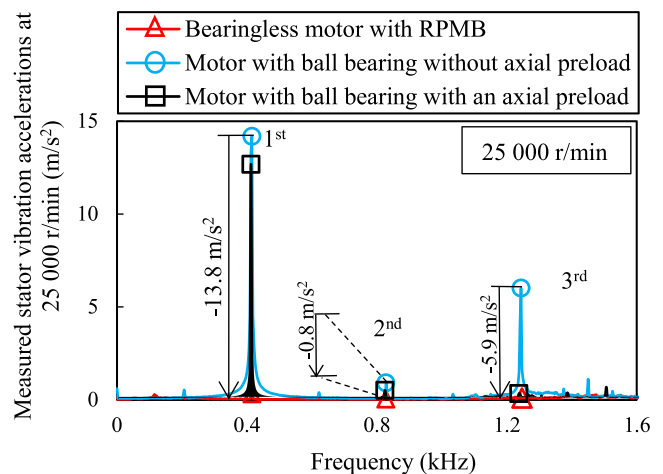[5] Estimation of ball bearing losses from Fig. 15.

FIGURE 16. Spectra of the measured stator vibration acceleration of the three test motors at 25 000 r/min.

winding. Only a set of three-phase winding that generates the rotating torque by q-axis current and axial force by d-axis current is available. However, at 14 000 r/min, the input power at a no-torque load, shown in Fig. 15, was measured to be 1.17 W, which included the motor iron loss, copper loss, windage loss, and suspension power loss. Therefore, the suspension power was less than 3.9% of the rated motor power.

3) FRICTIONAL LOSS OF BALL BEARIGS

The losses in ball bearings used for experiments was also investigated. The frictional loss of a ball bearing [29] is given by

$$F_b = M \times \omega_r \quad (12)$$

where

$$M = 0.5 \mu P d_m \quad (13)$$

where M is the frictional moment (N · m), μ is the coefficient of friction (0.08) steel to steel, P is the equivalent dynamic bearing load = 0.0023 kN, d_m is the mean bearing diameter (mm) = 7 mm, and ω_r is the rotational angular speed = 2618 rd/s at 25 000 r/min. In this study, at 25 000 r/min, the frictional loss of two ball bearings was calculated as 3.4 W using (12). In our previous paper [30], we measured the two ball bearing losses of 3.57 W without axial preload at 25 000 r/min. In this study, from Fig. 15, at 25 000 r/min, the input powers to the (i) bearingless motor with RPMB, (ii) motor with ball bearings without axial preload, and (iii) motor with ball bearings with axial preload were 2.7, 4.4, and 11.2 W, respectively. In addition, the suspension loss in the bearingless motor with RPMB was estimated to be approximately 1 W at 25 000 r/min. Thus, the input power without magnetic suspension loss of the bearingless motor was 1.7 W. Therefore, the ball bearing losses without and with axial preload were 2.7 and 9.5 W, respectively. We can observe the reasonable correspondence of 2.7 W to the calculated value of 3.4 W and measured ball bearing losses of 3.57 W in [30]. Therefore, the input power of the motor with ball bearings was higher

than that of the bearingless motor with RPMB owing to ball bearing frictional power loss. The power loss of ball bearings is proportional to the total frictional moment and rotational speeds. Especially, at high rotational speed, the power loss of ball bearings increases resulting in a high input power In addition, the results of ball-bearing losses in different evaluations are listed in Table 3.

C. MEASURED STATOR VIBRATION ACCELERATIONS
1) MEASUREMENT RESULTS OF STATOR VIBRATION ACCELERATION IN THREE TEST MOTORS

Fig. 16 shows the spectrums of the measured stator vibration acceleration of major components, these are fundamental, second, and third components of three test machines at 25 000 r/min. Bearingless motor with RPMBs has the notable reductions of the −13.8 and −5.9 m/s² at the fundamental and third components, respectively, compared with the motor with ball bearings without an axial preload.

Fig. 17 shows the experimentally measured fundamental frequency component of the radial stator vibration acceleration for the three test motors. At 3000 and 4000 r/min, the stator vibration acceleration of the bearingless motor was
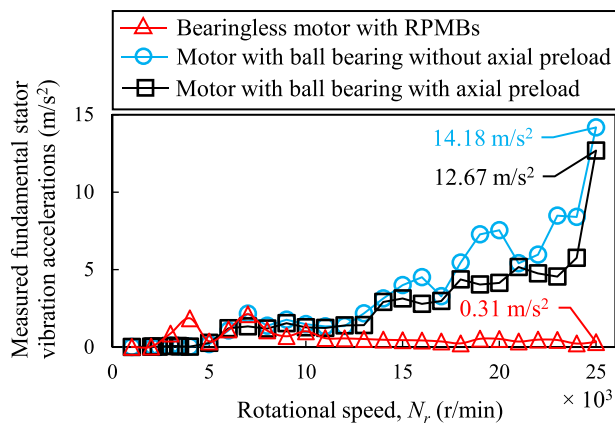
FIGURE 17. Experimentally measured fundamental stator vibration acceleration of the three test motors at up to 25 000 r/min.

FIGURE 18. Experimentally measured overall acoustic noise for the three test motors up to 25 000 r/min.

TABLE 4. Measurement Results of Input Power and Stator Vibration Acceleration At 25 000 r/min in Four Cases of the Test Motors

Cases	Input power (W)	Stator vibration (m/s^2)	Average d-axis current (A)
I	2.7	0.31	0.08
II	4.4	14.18	0
III	11.2	12.67	0
IV	7.2	11.82	2.72

Case I: the bearingless motor with RPMBs (see Fig. 7(a)).
Case II: the motor with ball bearings without axial preload (see Fig. 7(b)).
Case III: the motor with ball bearing with axial preload (see Fig. 7(c)).
Case IV: the motor with ball bearings with axial force caused by the d-axis current.

FIGURE 19. Spectrums of the measured sound pressure noise for the three test motors at 25 000 r/min with respect up to 1.6 kHz.

slightly high owing to the critical speed. In contrast, in the speed range of 8000 to 25 000 r/min, the bearingless motor was found to exhibit significantly low stator vibration acceleration. At 25 000 r/min, the stator vibration acceleration of the bearingless motor was only 2%. Furthermore, in the bearingless motor with RPMB, the simulation and experimental results of the stator vibration acceleration were 0.39 and 0.31 m/s^2 at 25 000 r/min, respectively. In addition, at 20 000 and 10 000 r/min, the simulation results of the stator vibration acceleration measured 0.45 and 0.9 m/s^2, respectively, while the experimental results were 0.52 and 1.0 m/s^2, respectively. For the motor with ball bearings, the stator vibration acceleration measured 25 m/s^2 in the simulation, while 14 m/s^2 was measured in the experiment at 25 000 r/min. In addition, at 20 000 and 10 000 r/min, the simulation results of the stator vibration acceleration were 8.0 and 0.3 m/s^2, respectively, while the experimental results were 7.5 and 1.5 m/s^2, respectively. Thus, slight discrepancies were observed.
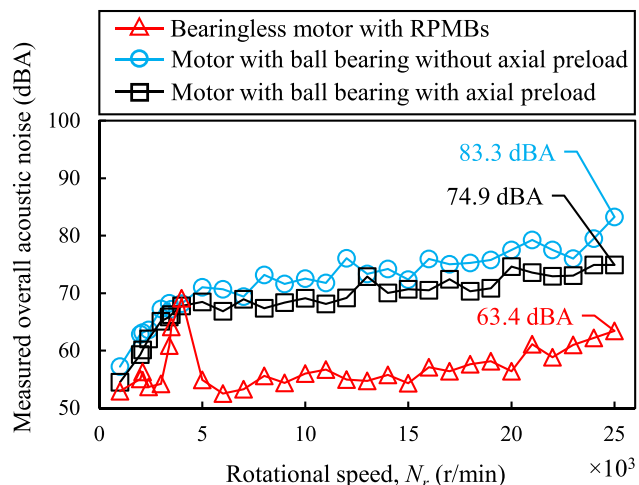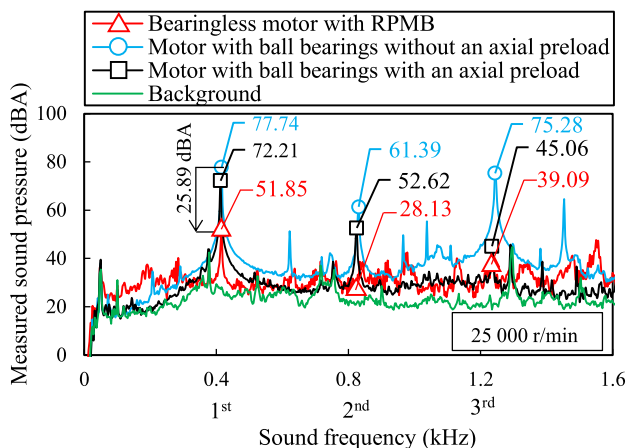
2) STATOR VIBRATION ACCELERATIONS AT LOW ROTATIONAL SPEED REGION
According to Fig. 17, there are different stator vibrations acceleration in the bearingless motor with RPBM and motors with ball bearings at low rotational speeds of 3000 to 4000 r/min. Thus, this different vibration was studied. The bearingless motor with RPMB had a critical speed for rotational speed ranging from 3000 to 4000 r/min. The natural frequency f_{rc} and the critical speed N_{rc} (r/min) in the radial motion can be calculated using (5), where k_{rs} and m_r can be populated from Table 1 and substituted in (5). The natural frequency was calculated as $f_{rc} = 55$ Hz. Thus, N_{rc} can be obtained as

$$N_{rc} = f_{rc} \times 60 = 3300 \text{ r/min.} \qquad (14)$$

Based on our experiment with a rotor shaft having a set of two RPMB, the rotor shaft was highly displaced or tilted in the radial direction when the motor was run at the critical
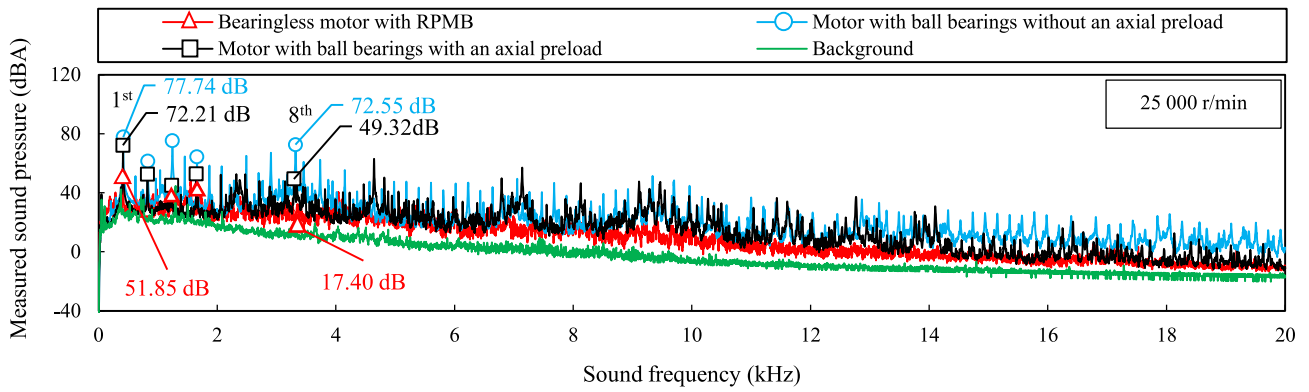
FIGURE 20. Spectra of the experimentally measured acoustic noise of the three test motors at 25 000 r/min with respect to frequency of up to 20 kHz.
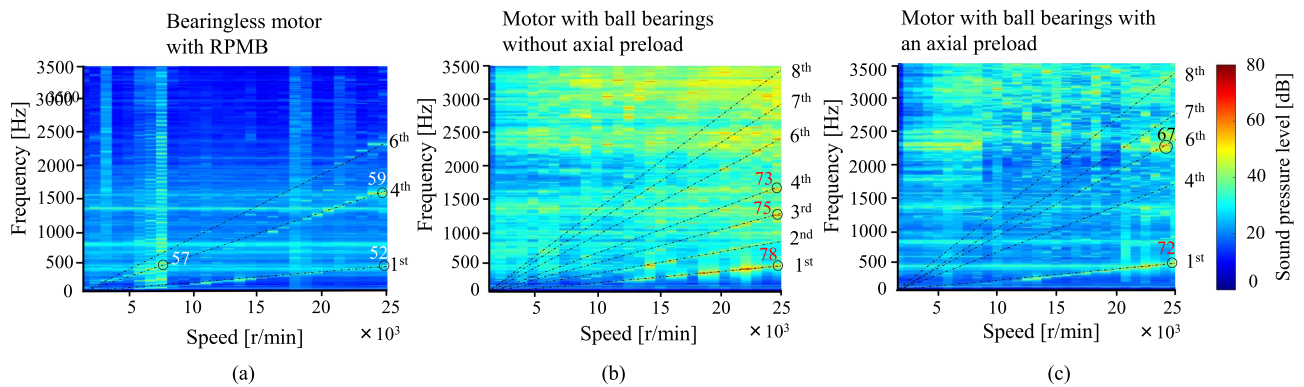

FIGURE 21. Experimentally measured sound pressure level for the three test motors: (a) bearingless motor with RPMBs (b) motor with ball bearings without a preload (c) motor with ball bearings with an axial preload.

speed. The critical speed exists in the rotational speed range. Thus, a high stator vibration acceleration was observed at the critical speed region in the bearingless motor. Conversely, the motor with ball bearings had no critical speed at the low-speed range of 3000–4000 r/min due to its high coupled rotor-stator stiffness k_{rs}. Therefore, only centrifugal force caused by the product of rotor mass and a square of the rotational speed causes stator vibration acceleration in the case of the motor with ball bearings.

3) COMPARISON OF INPUT POWER AND STATOR VIBRATION ACCELERATION IN FOUR CASES OF TEST MOTORS

The measured input power and stator vibration acceleration in four cases of test motors at 25 000 r/min are listed in Table 4. The experimental results show that Case I: bearingless motor with RPMB offers the lowest power consumption and stator vibration acceleration at 25 000 r/min when compared to the other test cases; even though the bearingless motor requires an average d-axis current of 0.08 A to keep the rotor in position. In Case II: a motor with ball bearings without axial preload, both input power and stator vibration acceleration have increased, while in Case III: a motor with ball bearings with axial preload, the stator vibration acceleration decreases by

adopting the spring-wave washer; however, the input power is significantly high. In Case IV: motor with ball bearings with axial force generation by injecting the rated d-axis current of 2.72 A, the stator vibration acceleration decreases up to 16.6% when compared to that in Case II without injecting the d-axis current. However, the input power also increases in Case IV.

D. MEASURED ACOUSTIC NOISE

Fig. 18 shows the experimentally measured overall acoustic noise in the three test motors. The overall acoustic noise level of the bearingless motor was significantly low. At 25 000 r/min, maximum reductions of 19.9 and 11.5 dBA were achieved when compared to the cases of the motor with ball bearings without and with axial preload, respectively. The highest overall acoustic noise in the bearingless motor occurred at 4000 r/min owing to the critical speed.

Fig. 19 shows the spectra of the experimentally measured acoustic noise with respect to frequency of up to 1.6 kHz for the three test motors at 25 000 r/min. The bearingless motor with RPMB showed a dominant acoustic noise reduction of 25.89, 33.26, and 36.19 dBA at fundamental, second, and third frequency components, respectively.

Fig. 20 shows an extended image of Fig. 19. The frequency range was extended up to 20 kHz with respect to the spectra of the measured acoustic noise for the three test motors at 25 000 r/min. The test results confirmed that the bearingless motor with RPMB had the least acoustic noise in the frequency range of up to 20 kHz when compared to those in the two motors with ball bearings. In addition, a maximum reduction up to 55.15 dBA at the eighth frequency component was observed when compared to that in the motor with ball bearings without an axial preload.

Fig. 21 shows the Campbell diagram of the measured sound pressure levels of the three test motors. The spectra of acoustic noise were measured at intervals of 1000 r/min and some high peaks were marked. Points higher than 70 dB, between 60 and 70 dB, and lesser than 60 dB are shown in red, black, and white fonts, respectively. Clearly, the acoustic noise level of the bearingless motor with RPMB was significantly low.

E. DISCUSSION

In this study, experiments were conducted to measure the input power consumption, acoustic noise, and stator vibration acceleration for three test motors. The motor with ball bearings without the axial preload had the highest acoustic noise and stator vibration acceleration in the high-speed regions. They were reduced by the axial preload of the spring-wave washer, but the amount of input power required increased. Conversely, the bearingless motor with RPMB was found to exhibit the lowest level of acoustic noise, stator vibration acceleration, and input power requirement at high rotational speeds.

VII. CONCLUSION

In this study, the acoustic noise, stator vibration acceleration, and input power of a one-DOF actively positioned single-drive bearingless motor with RPMB are compared to those of test motors with ball bearings. Experiments confirmed that the bearingless motor was found to reduce the acoustic noise, stator vibration acceleration, and input power requirement in the high-speed region. At a rotational speed of 25 000 r/min, the bearingless motor showed 19.9% lower overall acoustic noise, 97.82% lower stator vibration acceleration, and 37.95% lower power consumption when compared to those of the motor with ball bearings without axial load. In addition, the reason for the reduction was investigated by simulating a two-mass-spring system in MATLAB/Simulink. The bearingless motor with RPMB, composed of PM rings, allowed the radial movement of the rotor. Therefore, the stator vibration acceleration was reduced, which in turn reduced the acoustic noise. Thus, this article presents an example of a bearingless motor with RPMB that can realize reductions in acoustic noise, stator vibration, and input power consumption. Further study on the generalization of this concept can be performed.

REFERENCES

[1] M. Neff, N. Barletta, and R. Schob, "Bearingless centrifugal pump for highly pure chemicals," in *Proc. 8th Int. Symp. Magn. Bearing*, 2002, pp. 283–287.

[2] H. Hoshi, T. Shinshi, and S. Takatani, "Third-generation blood pumps with mechanical noncontact magnetic bearings," *Artif. Org.*, vol. 30, no. 5, pp. 324–338, 2006, doi: 10.1111/j.1525-1594.2006.00222.x.

[3] T. Reichert, T. Nussbaumer, and J. W. Kolar, "Investigation of exterior rotor bearingless motor topologies for high-quality mixing applications," *IEEE Trans. Ind. Appl.*, vol. 48, no. 6, pp. 2206–2216, Nov./Dec. 2012, doi: 10.1109/TIA.2012.2226853.

[4] T. Nussbaumer, P. Karutz, F. Zurcher, and J. W. Kolar, "Magnetically levitated slice motors—An Overview," *IEEE Trans. Ind. Appl.*, vol. 47, no. 2, pp. 754–766, Mar./Apr. 2011, doi: 10.1109/TIA.2010.2102731.

[5] E. Severson, R. Nilssen, T. Undeland, and N. Mohan, "Suspension force model for bearingless ac homopolar machines designed for flywheel energy storage," in *Proc. 7th IEEE GCC Conf. Exhib.*, 2013, pp. 274–279.

[6] H. Mitterhofer, B. Mrak, and W. Gruber, "Comparison of high-speed bearingless drive topologies with combined windings," *IEEE Trans. Ind. Appl.*, vol. 51, no. 3, pp. 2116–2122, May./Jun. 2015, doi: 10.1109/TIA.2014.2369820.

[7] Z. Liu, A. Chiba, Y. Irino, and Y. Nakazawa, "Optimum pole number combination of a buried permanent magnet bearingless motor and test results at an output of 60 kW with a speed of 37000 r/min," *IEEE Open J. Ind. Appl.*, vol. 1, pp. 33–41, 2020, doi: 10.1109/OJIA.2020.2975852.

[8] H. Sugimoto, I. Shimura, and A. Chiba, "Principle and test results of energy-saving effect of a single-drive bearingless motor in cooling fan applications," *IEEJ J. Ind. Appl.*, vol. 6, no. 6, pp. 456–462, 2017.

[9] A. Chiba, T. Fukao, O. Ichikawa, M. Oshima, M. Takemoto, and D. G. Dorrell, *Magnetic Bearing and Bearingless Drive*, London, U.K., Newnes, Elsevier. 2005.

[10] G. Munteanu, A. Binder, and S. Dewenter, "Five-axis magnetic suspension with two conical air gap bearingless PM synchronous half-motors," in *Proc. Int. Symp. Power Electron. Power Electron., Elect. Drives, Automat. Motion*, 2012, pp. 1246–1251.

[11] N. Yamamoto, M. Takemoto, S. Ogasawara, and M. Hiragushi, "Experimental estimation of a 5-axis active control type bearingless canned motor pump," in *Proc. IEEE Int. Mach. Drives Conf.*, 2011, pp. 148–153.

[12] H. Bleuler et al., "Micromachined active magnetic bearings," in *Proc. 5th Int. Symp. Magn. Bearing*, 1994, pp. 349–352.

[13] R. Schob and N. Barletta, "Principle and application of a bearingless slice motor," in *Proc. 5th Intl. Symp. Magn. Bearing*, 1996, pp. 313–318.

[14] J. Kuroki, T. Shinshi, L. Li, and A. Shimokohbe, "Miniaturization of a one-axis-controlled magnetic bearing," *Precis. Eng.*, vol. 29, no. 2, pp. 208–218, 2005, doi: 10.1016/j.precisioneng.2004.08.001.

[15] T. Ohji, Y. Katsuda, K. Amei, and M. Sakui, "Structure of one-axis controlled repulsive type magnetic bearing system with surface permanent magnets installed and its levitation and rotation tests," *IEEE Trans. Magn.*, vol. 47, no. 12, pp. 4734–4739, Dec. 2011, doi: 10.1109/TMAG.2011.2160403.

[16] J. Asama, Y. Hamasaki, T. Oiwa, and A. Chiba, "Proposal and analysis of a novel single-drive bearingless motor," *IEEE Trans. Ind. Electron.*, vol. 60, no. 1, pp. 129–138, Jan. 2013, doi: 10.1109/TIE.2012.2183840.

[17] H. Sugimoto, S. Tanaka, A. Chiba, and J. Asama, "Principle of a novel single-drive bearingless motor with cylindrical radial gap," *IEEE Trans. Ind. Appl.*, vol. 51, no. 5, pp. 3696–3706, Sep./Oct. 2015, doi: 10.1109/TIA.2015.2424883.

[18] H. Sugimoto, T. Srichiangsa, and A. Chiba, "Design of a high-speed single-drive bearingless motor," in *Proc. IEEE Int. Elect. Mach. Drives Conf.*, 2017, pp. 1–6.

[19] T. Srichiangsa, H. Sugimoto, and A. Chiba, "Torque density improvement of a one axis actively positioned single-drive bearingless motor," in *Proc. IEEE Energy Convers. Congr. Expo.*, 2018, pp. 6908–6913.

[20] W. Bauer and W. Amrhein, "Electrical design considerations for a bearingless axial-force/torque motor," *IEEE Trans. Ind. Appl.*, vol. 50, no. 4, pp. 2512–2522, Jul./Aug. 2014, doi: 10.1109/TIA.2014.2300415.

[21] T. Srichiangsa, H. Sugimoto, Y. Fujii, and A. Chiba, "Design, development, and experimental results of a 30 000-r/min one-axis actively positioned single-drive bearingless motor," *IEEE Trans. Ind. Appl.*, vol. 57, no. 6, pp. 6783–6791, Nov./Dec. 2021, doi: 10.1109/TIA.2021.3090736.

[22] Y. Yan, D. Zhiquan, Z. Qianying, and W. Xiaolin, "Stator vibration analysis of bearingless switched reluctance motors," in *Proc. Int. Conf. Elect. Control Eng.*, 2010, pp. 1993–1996.

[23] A. Sinervo and A. Arkkio, "Eccentricity related forces in two-pole induction motor with four-pole stator damper winding analyzed using measured rotor orbits," *IEEE Trans. Magn.*, vol. 49, no. 6, pp. 3029–3037, Jun. 2013.

[24] E. Marth, G. Jungmayr, and W. Amrhein, "Fundamental considerations on introducing damping to passively magnetically stabilized rotor systems," *Adv. Mech. Eng.*, vol. 8, no. 12, pp. 1–9, 2016.

[25] H. Sugimoto and A. Chiba, "Parameter identification of current-force factor and torque constant in single-drive bearingless motors with back EMF," *IEEE Trans. Ind. Appl.*, vol. 55, no. 5, pp. 4754–4761, Sep./Oct. 2019.

[26] H. Sugimoto, I. Shimura, and A. Chiba, "A novel stator structure for active axial force improvement in a one-axis actively positioned single-drive bearingless motor," *IEEE Trans. Ind. Appl.*, vol. 53, no. 5, pp. 4414–4421, Sep./Oct. 2017, doi: 10.1109/TIA.2017.2712567.

[27] RION CO., LTD, "Sound and vibration; web-support, Japan, Accessed: Jul. 20, 2022. [Online]. Available: https://rion-sv.com/download/catalog/UC-59

[28] RION CO., LTD, "Sound and vibration; web-support," Accessed: Jul. 20, 2022. [Online]. Available: https://rion-sv.com/download/catalog/PV-91C

[29] SKF CO., Swedish LTD Ball, "Bearing factory; web-support, United State," Accessed: Nov. 14, 2022. [Online]. Available: https://www.skf.com/us/products/rolling-bearings,

[30] T. Srichiangsa, H. Sugimoto, Y. Fujii, K. Kiyota, and A. Chiba, "Estimation of magnetic suspension loss in a 30000 r/min one-axis actively positioned single-drive bearingless motor," in *Proc. Int. Power Electron. Conf.*, 2022, pp. 401–406.

HIROYA SUGIMOTO (Member, IEEE) was born in Tokyo, Japan, in 1985. He received the B.S. and M.S. degrees in electrical engineering from the Tokyo University of Science, Tokyo, China, in 2007 and 2009, respectively, and the Ph.D. degree in electrical and electronic engineering from the Tokyo Institute of Technology, Tokyo, Japan, in 2018.

In 2009, he joined the Honda R&D Co., Ltd., Automobile R&D Center, Tochigi, Japan. From 2011 to 2019, he was Assistant Professor with the Tokyo Institute of Technology. Since 2019, he has been an Associate Professor with the Department of Electrical and Electronic Engineering, the School of Engineering, the Tokyo Denki University. His research interests include bearingless motors, magnetic bearings, and high-speed machines.

Dr. Sugimoto is a Member of the *Institute of Electrical Engineering of Japan* (IEEJ) in Japan.

THEERAPHONG SRICHIANGSA (Member, IEEE) was born in Udon Thani Province, Thailand. He received the B.E. and M.E. degrees in electrical engineering from the King Mongkut's University of Technology Thonburi (KMUTT), Bangkok, Thailand, in 2008 and 2011, respectively. He received D.Eng. degree in electrical and electronic engineering from Tokyo Institute of Technology, Tokyo, Japan, in 2022.

During his D.Eng study from Oct 2016 to Sep 2022, he conducted research on one-DOF actively positioned bearingless motors and some parts of this study in this article have been carried out at Tokyo Institute of Technology. Since Oct 2022, he has been a Lecturer with the Department of Electrical Engineering, Faculty of Engineering, Sriracha, Kasetsart University, Thailand. His research interests include bearingless motors, magnetic bearings, and high-speed machines.

Dr. Srichiangsa is a Member of the *Institute of Electrical Engineering of Japan* (IEEJ) in Japan.

SURYA NARAYANA GUNDA was born in Pattikonda, India, in 1988. He received the Bachelor of Technology degree in electrical and electronics engineering from Jawaharlal Nehru Technological University Anantapur, India, in 2009. He is currently working toward the master's degree in electrical and electronic Engineering with the Department of Electrical and Electronic Engineering, School of Engineering, Tokyo Institute of Technology, Tokyo, Japan.

He has 10 years of work experience related to Train operations, Rolling Stock Maintenance, Construction, Commissioning, Operation, and Maintenance of a 25 kV Traction distribution network of the Indian Railway, India. His research interests include Bearingless motors, magnetic bearings, high-speed drives, and magnetically suspended machines.

YUSUKE FUJII (Member, IEEE) was born in Tottori, Japan, in 1990. He received the B.S., MS., and Ph.D. degrees in mechanical engineering from the Department of Mechanical Engineering, Shizuoka University, Hamamatsu, Japan, in 2015, 2017, and 2020, respectively.

Since 2020, he has been an Assistant Professor with the Department of Electrical and Electronic Engineering, the Tokyo Institute of Technology, Tokyo, Japan. His research interests include bearingless motors, magnetic bearings, and motor drives.

Dr. Fujii is a Member of the *Institute of Electrical Engineers of Japan* (IEEJ), and the *Japan Society of Mechanical Engineers* (JSME).

KYOHEI KIYOTA (Member, IEEE) received the B.S., M.S., and Ph.D. degrees in electrical and electronic engineering from the Department of Electrical and Electronic Engineering in the School of Engineering, Tokyo Institute of Technology, Tokyo, Japan, in 2011, 2013, and 2015, respectively.

From 2013 to 2016, he was a Research Fellow of the Japan Society for the Promotion of Science. In 2015, he joined as a Research Member with the Department of Electrical and Electronic Engineering in the School of Engineering, Tokyo Institute of Technology, Tokyo, Japan. In 2016, he joined as a Specially Appointed Assistant Professor with the Graduate School of Science and Engineering for Research, University of Toyama, Toyama, Japan. Since 2020, he has been an Associate Professor with the School of Engineering, Tokyo Institute of Technology, Tokyo, Japan. His research interests include switched reluctance motors, synchronous reluctance motors and bearingless motors.

Dr. Kiyota is a Member of the *Institute of Electrical Engineers of Japan* (IEEJ).

JUNICHI ASAMA (Member, IEEE) was born in Niigata, Japan, in 1979. He received the B.S., M.S., and Ph.D. degrees in mechanical engineering from the Tokyo Institute of Technology, Tokyo, Japan, in 2002, 2004, and 2006, respectively.

He was a Postdoctoral Researcher with Precision and Intelligence Laboratory, Tokyo Institute of Technology, in 2006, a Research Associate with the Department of Electrical Engineering, Tokyo University of Science, Chiba, Japan, in 2007. Since 2009, he has been an Associate Professor with the Department of Mechanical Engineering, Shizuoka University, Hamamatsu, Japan. His research interests include bearingless motors and permanent magnet motor drives.

Dr. Asama is a Member of the *Institute of Electrical Engineers of Japan*, the *Japan Society for Precision Engineering*, and the *Japan Society of Mechanical Engineers*.

AKIRA CHIBA (Fellow, IEEE) received the B.S., M.S., and Ph.D. degrees in electrical engineering from the Tokyo Institute of Technology, Tokyo, Japan, in 1983, 1985, and 1988, respectively.

In 1988, he joined the Tokyo University of Science as a Research Associate with the Department of Electrical Engineering, Faculty of Science and Technology. Since 2010, he has been a Professor with the School of Engineering, Tokyo Institute of Technology, Tokyo, Japan. He has been studying magnetically suspended bearingless ac motors, super high-speed motor drives, and rare-earth-free-motors for automotive traction applications. He has so far authored or coauthored more than 1170 papers including the first book on "Magnetic Bearings and Bearingless Drives" in 2005.

Prof. Chiba was the recipient of the First Prize Paper Award from the Electrical Machine Committee in the IEEE IAS in 2011 on a rare-earth-free motor, the second and third place Best Paper Awards in IEEE Transactions on Energy Conversion in 2016 and 2017, respectively, the IEEJ Prize Paper Awards in 1998, 2005, 2018, and 2020 Nikola Tesla Award, one of IEEE Technical Field Awards. He was a Secretary, Vice-Chair, Vice-Chair-Chair-Elect, Chair, and Past-Chair in the Motor Sub-Committee in the IEEE PES during 2007–2016. He was a Member, Chair, and Past-Chair in the IEEE Nikola Tesla Field Award Committee in 2009–2014. He served as a Chair in IEEE-IAS Japan Chapter in 2010–2011. He was ECCE Vice-Chair in technical committee during 2016–2019. He was Technical Co-Chair in IEEE IEMDC 2017 held in Miami, FL, USA. He is TCPRC and was an Associate Editor for the IEEE TRANSACTIONS ON INDUSTRY APPLICATIONS since 2020 and from 2011 to 2019, respectively. He was Founding Chair in the Motor Technical Committee in Japan Society of Automotive Society in 2012–2018. He has served as Secretary, Vice Chair, Chair, and Past-Chair in IEEE-IAS Electric Machine Committee since 2016. He has served as an Editor for the IEEE TRANSACTIONS ON ENERGY CONVERSION since 2013. He was the IEEE IAS Fellow Committee Executives from 2017 to 2020. He has been the Chair in IEEJ Electric Machine Committee since 2020. He has served as Examiner in the Nagamori Award since 2015. He was the Department Head of Electrical and Electronics Department during 2014 and 2016 and led MOOC project of the introduction of Electrical and Electronics Engineering, released in May 2017 through EDX. He has led active learning with internet Handbook application in undergraduate and graduate course lectures.